



Non-uniform fiber-resin distributions of pultruded GFRP profiles

Peng Feng^{*}, Yuwei Wu, TianQiao Liu

MOE Key Lab of Civil Engineering Safety and Durability, Department of Civil Engineering, Tsinghua University, Beijing, 100084, China

ARTICLE INFO

Keywords:

Glass fiber reinforced polymer (GFRP) profiles
Non-uniform fiber-resin distribution (NUFRD)
Initial imperfection
Pultrusion

ABSTRACT

Pultruded fiber reinforced polymer (FRP) composite profiles are usually regarded as the transverse-isotropic material based on the assumption that the fiber and resin are uniformly distributed across the profile sections. However, this is practically not the case due to the limitations of the pultrusion technology. The non-uniform fiber-resin distribution (NUFRD), as a type of inherent initial imperfection for pultruded glass fiber reinforced polymer (GFRP) profiles, was investigated. The resin contents of 49 different pultruded GFRP sections were tested and analyzed. The standard calcination method was used to measure the resin content. The sections were provided by three different manufactures and included the I-sections, box-sections, angle-sections, circular tubes, channel-sections and flat plates. Multiple sampling locations were specified for each type of section. The test results showed that the degree of NUFRD for each type of section is different. In particular, the I-sections showed the most significant material non-uniformity. The largest COV (coefficient of variation) of the measured resin contents is 0.16. Additionally, the influence of NUFRD on the mechanical properties of GFRP members was addressed. The material non-uniformity would increase the initial section eccentricity. Finite element models were built to simulate the compressive GFRP members. It was found that the critical buckling loads of GFRP compressive members will be reduced due to NUFRD.

1. Introduction

Pultruded glass fiber reinforced polymer (GFRP) composites have been widely used in the world because of their advantages such as high strength-to-weight ratio, good corrosion resistance, wide variety of cross-section shapes, and ease of construction [1–6]. Pultruded GFRP composites have been applied in many engineering applications, such as pedestrian bridges [7–13] and residential buildings [14]. The acceptance of pultruded GFRPs has also been significantly improved after being researched and practiced for decades. To date, many advanced theoretical methods have been proposed to analyze the structural behavior of pultruded GFRPs, most of which were based on the assumption of uniformly distributed fiber and resin across the profile sections, also referred to as the transverse-isotropic nature at material cross-sections [15–17].

The fabrication process of pultruded fiber reinforced polymer profiles, namely pultrusion, is a continuous process with high efficiency. The typical pultrusion process of an I-section profile is shown in Fig. 1. The fibers, in the form of fiber rovings, are pulled forward by a pulling system. The fiber rovings and continuous strand mats (CSMs) are first immersed into the resin at the resin impregnator. Then, in preforming

stage, the fiber rovings and CSMs are pulled through a distribution plate (with many holes) to position the fiber rovings. Finally, all materials are pulled into the mold, where the resin is heated and cured. After being pulled out of the mold, the cured GFRP profiles will cool down and contract [18–20].

This manufacturing process will lead to some unique characteristics of pultruded GFRPs. For instance, some initial imperfections may be introduced [21,22]. Baran et al. [23] investigated the residual stress and geometric variations generated in the pultrusion process. In their study, the effects of thermal anisotropy, polymerization/crystallization shrinkage, tool-part interaction, resin flow and compaction, fiber wrinkling, and temperature gradients were discussed. For pultrusion process, Baran et al. [24,25] reported that the non-uniform temperature and the varying degree of curing were the main causes of the residual stresses and geometric distortions. In addition, because of the manufacturing process, pultruded GFRPs have a unique micro-structure at the nanometer level [26–28].

In this paper, the photos of the cross-sections of a pultruded GFRP I-section profile were taken at three levels, as shown in Fig. 2, including the structural level, meso level and micro level. The structural level image was taken by the camera Canon EOS 70D; the meso-level image

^{*} Corresponding author.

E-mail addresses: fengpeng@tsinghua.edu.cn (P. Feng), wyw16@mails.tsinghua.edu.cn (Y. Wu), liu_tianqiao@mail.tsinghua.edu.cn (T. Liu).

<https://doi.org/10.1016/j.compositesb.2021.109543>

Received 2 September 2021; Received in revised form 29 October 2021; Accepted 28 November 2021

Available online 30 November 2021

1359-8368/© 2021 Elsevier Ltd. All rights reserved.

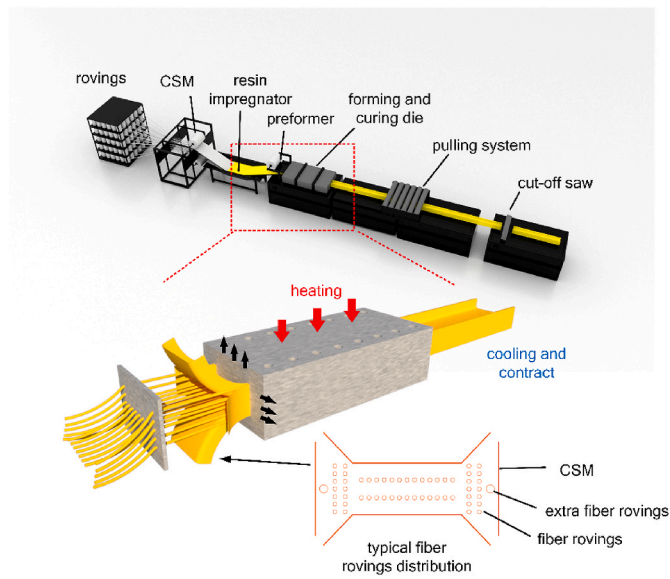


Fig. 1. Typical pultrusion process of GFRP I-section profile.

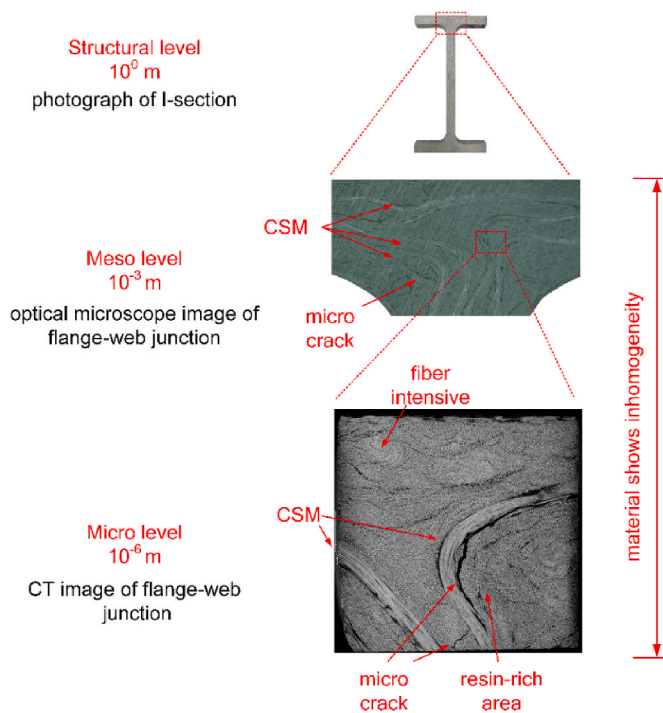


Fig. 2. Cross-sections of a pultruded GFRP I-section profile taken at three levels.

was taken by optical microscope (Zhiqi-601) with a magnification factor of 135; and the micro-level image was taken by computed tomography (CT) with the distinguishability of 6.35 μm , provided by Sanying Motion Control Instruments Ltd. The pultruded GFRP profile seems to have a good and uniform fiber-resin distribution in the structural level image, but the CT photo taken at the micro level clearly shows that the imperfections indeed exist, including the micro cracks and the non-uniform distribution of fibers and resin.

The micro cracks, shown in Fig. 2, are mainly due to the waviness of the CSM, the temperature effect and the resulting non-uniform contraction at cooling stage [29]. The other notable imperfection is the non-uniform distribution of fibers, which can further lead to the fiber

intensive areas and resin-rich areas. The fiber intensive areas show a more intensive white color in Fig. 2 and have larger fiber density, while the resin-rich areas show a less intensive white color. The fiber fraction is directly related to the overall mechanical property of pultruded GFRPs. Thus, the non-uniform fiber-resin distribution (NUFRD), which is an inherent characteristic of pultruded profiles induced by the manufacturing process, can result in the variation of mechanical properties across the section. Such a non-uniform distribution was also mentioned in other studies. Baran et al. [30] characterized the internal geometry of a pultruded FRP by X-ray micro-CT. The resin-rich areas and discontinuous porosity were observed. Such imperfections are influential to the mechanical properties of pultruded GFRPs, including the strength and modulus in both longitudinal and transversal directions and should be considered in structural analysis and design [31–33]. Poulton and Sebastian [34] investigated the fiber mat misalignments of a multi-celled pultruded GFRP deck. These misalignments were classified, including the mat warping errors, resin injection, roving shifting and mat gaps. In addition, the fiber mat misalignments at web-flange junctions were reported to significantly impact the local buckling loads of pultruded GFRP beams [35–39].

The effect of imperfections has been considered by a Chinese standard, GB/T 31539-2015 [53]. In this standard, the full-section compressive test is prescribed. The compressive strength of the full-section is typically lower than that obtained from the coupon test (ASTM D6641-2009 [50]; GB/T 1448-2005 [51]), thus yielding a gap between full-section strength and coupon strength. This gap reflects the extent of imperfection of a GFRP section. GB/T 31539-2015 stipulates that the ratio of full-section compressive strength to coupon compressive strength shall be higher than 0.85.

In general, the studies and standards have confirmed that imperfections exist objectively in pultruded FRP. However, the degree of imperfection and its influence on mechanical properties have not been investigated quantitatively. In this work, the influence of NUFRD is quantitatively analyzed. The resin weight content is selected as the criterion to measure the material uniformity of pultruded GFRP profiles. Resin content as a representative parameter to quantitatively describe NUFRD is easy to be measured and is related to fiber volume content, which can be directly used to calculate the material mechanical properties. The six types of GFRP profiles from three manufacturers were experimentally measured and statistically analyzed. NUFRD resulting shift of section geometric center was calculated. Then, the effects of NUFRD for GFRP axial-compressive members were investigated based on the finite element analysis.

2. Experimental program

2.1. Test method

The calcination method was used to measure the resin content (GB/T 2577-2005 [52]; ISO 1172:1996 [54]). The calcination process is schematically shown in Fig. 3. In the first step, coupons were cut by an electric saw with a diamond blade from the specified positions of all sections. All coupons had the geometries smaller than $25 \times 25 \times 5$ mm (see the following section for detailed coupon geometries) and the weights smaller than 5 g. The geometries and weights were determined in accordance with standard tests (GB/T 2577-2005; ISO 1172:1996) so as to ensure the coupons can be calcinated completely. After cutting process, coupons were cleaned using ethyl alcohol and dried in a desiccator for 24 h. In the second step, the coupons and the crucible were weighted using an electronic balance. The weight of the crucible was recorded as m_1 , and the total weight of crucible and coupon was recorded as m_2 . In the third step, the crucible with the coupon was heated in a muffle furnace (SX-2 model, maximum heating temperature of 1000 $^{\circ}\text{C}$ and distinguishability of 1 $^{\circ}\text{C}$). Coupons were preheated at a temperature of 400 $^{\circ}\text{C}$ for 30 min, and then, heated at a temperature of 625 $^{\circ}\text{C}$ until the carbonaceous residue is reduced to ash. In the fourth

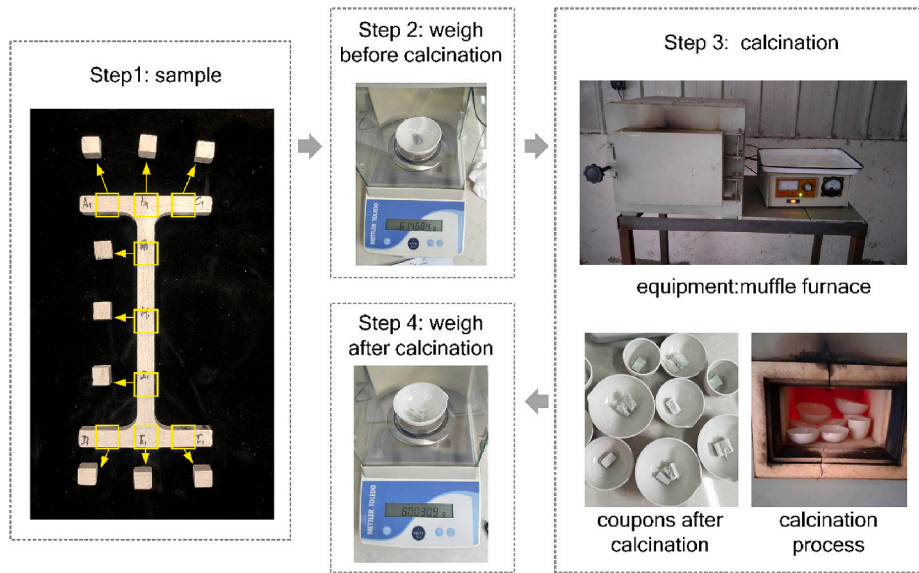


Fig. 3. Calcination process.

step, the remained material and crucible were weighted at room temperature, and the weight was recorded as m_3 . Finally, the resin content M_r can be calculated via Eq. (1).

$$M_r = \frac{m_2 - m_3}{m_2 - m_1} \quad (1)$$

2.2. Specimens

A total of 49 different pultruded GFRP sections were tested, including 6 I-sections, 16 box-sections, 7 angle-sections, 11 channel-sections, 6 circular tubes, and 3 flat plates. In order to account for the possible discrepancies between different manufacturers, these GFRP sections were provided by three manufactures in China, which are denoted as M1, M2 and M3, respectively. With that being said, raw materials are collected. The fiber type of all specimens is alkali-free glass fiber. The geometries of 49 GFRP sections and resin types are presented in Table 1. The weight fraction of fillings is small (much less than 5%, in this case), and thus, it is ignored in this work. It is noted that these factors, such as fillers, additives, and CSMs, may be considered in the future research [40–43].

Coupons for calcination tests were cut from the specified locations of each type of section, as shown in Fig. 4. The sampling location is chosen to cover every ply and be representative. For I-sections, nine locations were sampled, including three at the web (with equal spacing), two at web-flange junctions, and four at the midpoints of top and bottom flanges. For box-sections, eight locations were sampled, including four at the web-flange junctions, and four at the midpoints of flanges and webs. For angle-sections, three locations were sampled, including one at the junction and two at the midpoints of the legs. For circular tubes, eight locations were sampled, which were evenly spaced around the section. For channel-sections, seven points were sampled, including three at the web (with equal spacing), two at the web-flange junctions, and two at the midpoints of top and bottom flanges. For plates, five locations were sampled (with equal spacing). It is noted that for some sections with relatively small geometries, certain sampling locations were not used in the tests. The actual sampling locations of each GFRP section are shown in Appendix A. For each of the 49 sections, three coupons were obtained from one sampling location, thus permitting three repeated tests. The coupon designations are presented in Fig. 4.

3. Experimental results

3.1. Measured resin content

Detailed test results are presented in Appendix A. In these tables, the mean values (i.e., resin weight contents) of three repeated tests are shown. The coefficient of variation (COV) was calculated based on the resin contents measured at all sampling locations across a section. The experimental findings are as follows:

- The resin contents of six I-section profiles vary from 20.6% to 29.8%, with the average resin content of 26.8%, which is relatively low among all six types of GFRP sections. The COVs of resin contents of I-sections vary from 0.03 to 0.16, with an average value of 0.10.
- The resin contents of 16 box-section profiles vary from 20.8% to 35.7%, with the average resin content of 30.3%. The COVs of resin contents of box-sections vary from 0.01 to 0.12, with an average value of 0.05.
- The resin contents of seven angle-section profiles vary from 23.9% to 34.8%, with the average resin content of 30.29%. The COVs of resin contents of angle-sections vary from 0.01 to 0.04, with an average value of 0.03. It is evident that the COVs of angle-sections are much smaller than those of I- and box-sections, thus demonstrating the section shape of an angle could permit a more uniform fiber-resin distribution.
- The resin contents of six circular tubes vary from 18.2% to 32.7%, with the average resin content of 29.1%. The COVs of resin contents of circular tubes vary from 0.01 to 0.06, with an average value of 0.03.
- The resin contents of 11 channel-section profiles vary from 22.6% to 36.6%, with the average resin content of 30.0%. The COVs of resin contents of channel-sections vary from 0.02 to 0.09, with an average value of 0.05.
- The resin contents of three plates vary from 20.76% to 31.3%, with the average resin content of 25.7%. The COVs of resin contents of plates vary from 0.01 to 0.05, with the average value of 0.03.

In summary, I- and box-sections have the largest COVs, by up to 0.16 and 0.12, respectively, thus demonstrating the greatest extent of NUFRDs. All other sections have COVs less than 0.10, showing a relatively good uniformity of fiber-resin distribution.

Table 1
Geometries of pultruded GFRP sections.

Section type	Section number	Size/mm	Manufacturer	Resin type
I-section ($h \times b \times t$)	1	100 × 70 × 6	M 2	epoxy
	2	102 × 51 × 6.4	M 1	vinyl ester
	3	120 × 70 × 8	M 2	epoxy
	4	152 × 76 × 6.35	M 1	epoxy
	5	152 × 80 × 10	M 1	epoxy
	6	200 × 100 × 9.5	M 1	epoxy
box-section ($h \times b \times t$)	1	25 × 25 × 3	M 1	epoxy
	2	50 × 25 × 3	M 1	epoxy
	3	75 × 35.5 × 6	M 1	epoxy
	4	38 × 38 × 3.2	M 1	epoxy
	5	38 × 38 × 5	M 1	epoxy
	6	44 × 44 × 6	M 1	epoxy
	7	50 × 50 × 4	M 2	epoxy
	8	50.8 × 50.8 × 3.2	M 1	epoxy
	9	50.8 × 50.8 × 6.35	M 3	epoxy
	10	60 × 60 × 4.25	M 1	epoxy
	11	68 × 95 × 6	M 1	epoxy
	12	76.2 × 76.2 × 6.35	M 1	epoxy
	13	76.2 × 76.2 × 6.35	M 2	vinyl ester
	14	82 × 82 × 6.35	M 1	epoxy
	15	101.6 × 101.6 × 6.35	M 2	vinyl ester
	16	101.6 × 101.6 × 6.35	M 1	epoxy
angle-section ($h \times b \times t$)	1	50 × 50 × 3	M 1	epoxy
	2	50.8 × 50.8 × 6.35	M 2	epoxy
	3	55 × 55 × 4	M 3	epoxy
	4	75 × 75 × 6	M 1	epoxy
	5	75 × 75 × 10	M 1	epoxy
	6	100 × 100 × 8	M 1	epoxy
	7	101.6 × 101.6 × 6.35	M 1	vinyl ester
circular tube ($D \times t$)	1	25 × 2.5	M 1	epoxy
	2	30 × 2	M 1	epoxy
	3	38 × 3	M 1	epoxy
	4	40 × 4	M 2	epoxy
	5	48.5 × 6.75	M 1	epoxy
	6	82 × 3	M 1	epoxy
channel-section ($h \times b \times t$)	1	35 × 23 × 4.5	M 1	epoxy
	2	41.5 × 41.5 × 3.5	M 1	epoxy
	3	76.2 × 25 × 6.35 × 6.35	M 1	vinyl ester
	4	76.2 × 25 × 6.35	M 1	epoxy
	5	88.9 × 38.1 × 4.76	M 1	vinyl ester
	6	139.7 × 63.5 × 6.35	M 1	vinyl ester
	7	150 × 50 × 6	M 1	epoxy
	8	152.4 × 42.9 × 9.5 × 9.5	M 1	vinyl ester
	9	200 × 60 × 8	M 1	epoxy
	10	200 × 60 × 8	M 1	epoxy
	11	280 × 70 × 12	M 1	epoxy
plate ($b \times t$)	1	40 × 5	M 1	epoxy
	2	76.2 × 12.7	M 1	vinyl ester
	3	136 × 6.35	M 1	epoxy

3.2. Relative deviations

To analyze the variation of resin content across each GFRP section, the relative deviations (R) of resin contents measured at all sampling locations were calculated, as Eq. (2):

$$R_i = \frac{M_{r,i} - M_{r,avg}}{M_{r,avg}} \quad (2)$$

where R_i is the relative deviation of the resin content of i th sampling

location of a GFRP section; $M_{r,i}$ is the resin content measured at i th sampling location; and $M_{r,avg}$ is the average resin content of a GFRP section. The positive R_i value indicates that the resin content at i th location is higher than the average value of the entire section, while the negative R_i value indicates that the resin content at i th location is lower than the section average.

For each type of GFRP section except for plate (i.e., I-section, box-section, angle-section, channel-section, and circular tube), the average relative deviation at i th location $R_{i,avg}$ was calculated. Fig. 5 shows the calculated average relative deviations of resin contents at all sampling locations of those GFRP sections (plates are not shown due to limited data available). In this figure, the calculated average relative deviations at sampling locations are plotted, as shown in the line graphs (error bar indicates one standard deviation). The contour map shows the average relative deviations of entire section, in which the resin contents between sampling locations were obtained by linear interpolations.

From Fig. 5, I-section and box-section show much higher relative deviations of resin contents, while angle-section, circular tube and channel-section have smaller relative deviations. In particular, for I-sections, the resin contents at the webs is the highest, followed by web-flange junctions, and the resin contents at the flanges are the lowest. Surprisingly, the top flanges have much higher resin contents than those of bottom flanges, by up to 20% as shown in Fig. 5a. The top flange and bottom flange shall be theoretically symmetrical to each other, and the observed differences mainly result from the fluctuation in pultrusion process. However, the exact reason causing such a fluctuation is unknown, as it is essentially related with the state-of-practice of manufacturing which is not unfolded to public. On the other hand, the relative deviations are also large, which are in the range of 5%–13%. The reasons for NUFRD of I-section are not determined, which may include the dislocations of fiber rovings during manufacturing process. An example lay-up of I-section is shown in Fig. 6. The CSMs may have many wrinkles, especially in the flange-web junction. Those wrinkles of CSMs could lead to the dislocations of fibers, which further leads to non-uniform resin content.

For box-sections, as shown in Fig. 5b, the relative deviation at one corner (+5.7%) is much higher than the other sampling points. The standard deviations are less than 8%. In summary, resin content of box-sections is more uniform than that of I-sections. The higher resin content at one corner may result from the overlap and wrinkle of CSMs, which may lead to dislocations of the continuous fibers.

For circular tubes, as shown in Fig. 5d, the relative deviations are less than those of box-sections and I-sections. The relative deviations are smaller than 4%. Meanwhile, the standard deviations are less than 4%. Compared with box-sections, circular tubes evidently have a more uniform resin content. Such a discrepancy may result from the corners of box-sections. It is speculated that the corner (i.e., junction) has a negative impact on the uniform distribution of fiber and resin.

Angle-sections and channel-sections all have small relative deviations, as shown in Fig. 5c and e. The average relative deviations are within $\pm 5\%$ at all sampling points. Additionally, the standard deviations are smaller than 5%. The results show that angle- and channel-sections have the most uniform fiber-resin distribution. Although the shape of angle- and channel-sections is essentially similar to that of I-section, the relative deviations of angle- and channel-sections are much smaller. The reason is that the lay-ups of angle- and channel-sections are simpler; that is, the CSMs are parallel and continuous through the thickness of each section plate so that fewer wrinkles of CSMs exist in angle- and channel-sections.

3.3. Distributions of relative deviations

In addition to the relative deviations of resin contents across the GFRP sections, the distributions of relative deviations were investigated. The number of tests (denoted as frequency) is plotted against the relative deviations, as shown in Fig. 7. The height of each column reflects the

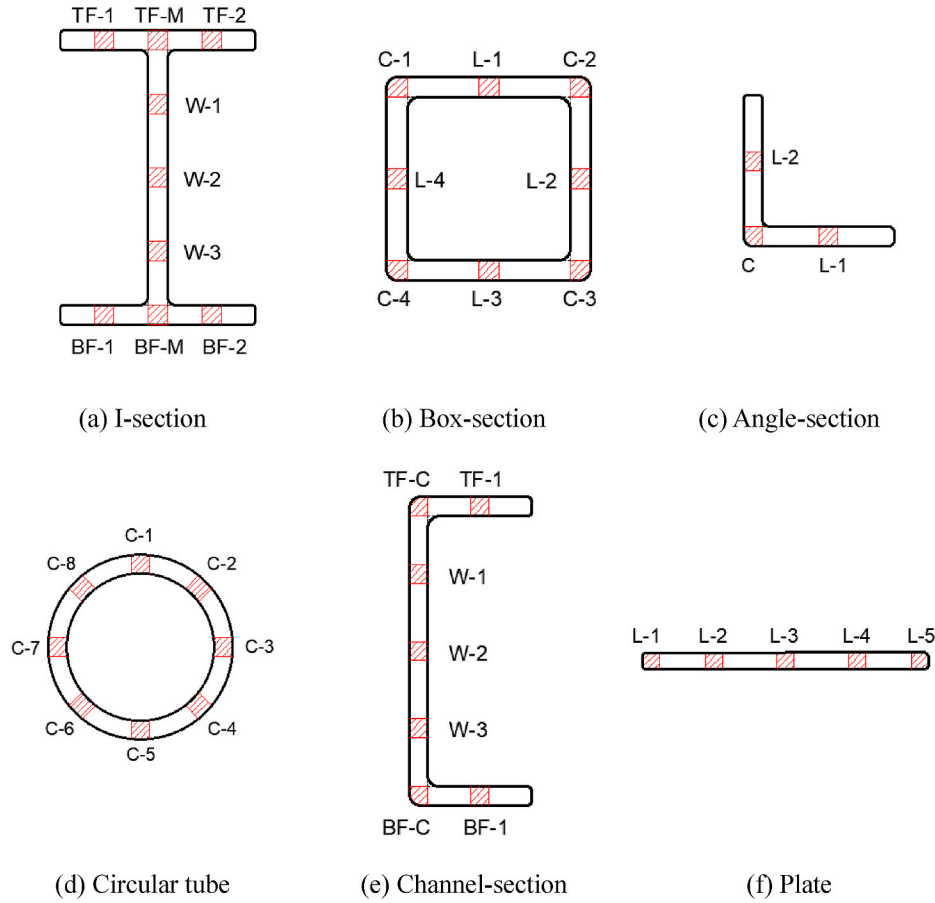


Fig. 4. Sampling locations of different GFRP sections.

frequency of tests that falls within the specified range of relative deviations. In this case, $\pm 2\%$ is selected as the increment size for relative deviation. Then, all the sub-distributions of relative deviations pertaining to I-sections, box-sections, angle-sections, circular tubes, and channel-sections were added up, yielding the overall distribution of relative deviations of resin contents of all five GFRP sections, as shown in the first plot (labeled as Summary) in Fig. 7. Finally, a normal distribution was applied to fit the summarized result of all five sections.

From Fig. 7, it can be seen that the overall distribution of relative deviations of resin contents of five pultruded GFRP sections correlates well with the standard normal distribution, with R^2 value = 0.94. The overall standard deviation of resin contents of all five GFRP sections is calculated as 7.10. However, different sections have distinct fiber-resin distributions. The standard deviations of resin contents of I-sections, box-sections, angle-sections, circular tubes, and channel-sections are 11.83, 6.33, 3.32, 3.73, and 5.39, respectively. These values are also reflected by the distributions shown in Fig. 7. For instance, the relative deviations of I-sections are distributed in a larger range than that of any other sections, thus showing the highest standard deviation when fitted by the normal distribution.

4. Analytical program

4.1. Resin-rich parameter

High resin content will lead to the reduced mechanical property, so that the resin-rich areas are the low-strength area of a section. In order to evaluate the degree of such resin richness, a parameter ρ is proposed, which is equal to the ratio of $M_{m,max}$ to $M_{m,avg}$ (as shown in Eq. (3)).

$$\rho = \frac{M_{m,max}}{M_{m,avg}} \quad (3)$$

where $M_{m,max}$ is tested maximum resin content of a section (i.e., a specimen); $M_{m,avg}$ is average resin content of this specimen. The resin-rich parameter ρ of tested 49 groups of data are calculated, and the results are shown in Fig. 8. It shows that all specimens have average resin-rich parameter ρ of 1.076, with a COV of 0.048. The ρ values of I-sections and box-sections are higher than these of the other types of sections. The parameter ρ is related to the degree of low-strength area of GFRP profiles. Based on the calculated ρ values, the reductions of the mechanical property in resin-rich area are analyzed in section 4.3.

4.2. Mechanical property determinations

NUFRD directly impacts the overall mechanical properties of GFRP composites. In this work, the measured fiber-resin distribution is used to determine the overall mechanical properties of GFRP composites. Besides, this method agrees well with almost all existing design guides that the mechanical properties of pultruded GFRP profiles are calculated concerning for their cross-sectional fiber-resin distributions/content. With that being said, the possible variations in the longitudinal direction of material are neglected. In classic equations for calculating the mechanical properties of GFRP composites, resin weight content M_m shall be transformed to fiber volume content V_f , as Eq. (4):

$$V_f = \frac{(1 - M_m)\rho_m}{M_m\rho_f + (1 - M_m)\rho_m} \quad (4)$$

where ρ_m is the density of resin; and ρ_f is the density of fiber.

To predict the longitudinal elastic modulus E_1 and major Poisson's

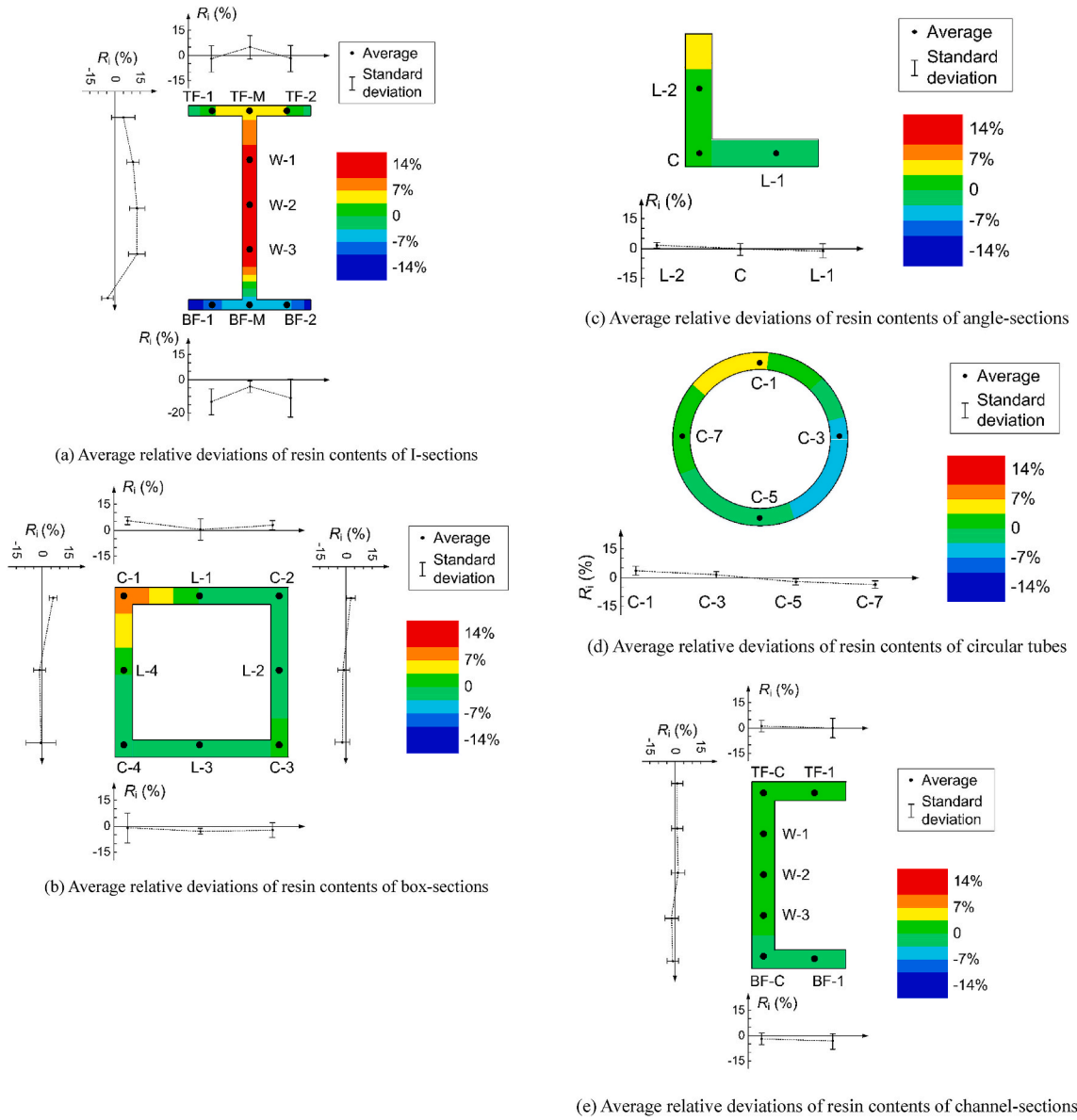


Fig. 5. Average relative deviations of resin contents of GFRP sections.

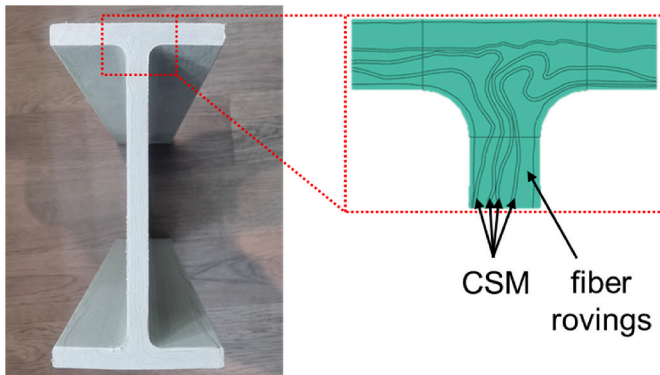


Fig. 6. Example lay-up of I-section.

ratio ν_{12} , Eq. (5) and Eq. (6) are used.

$$E_1 = E_f V_f + E_m (1 - V_f) \quad (5)$$

$$\nu_{12} = \nu_f V_f + \nu_m (1 - V_f) \quad (6)$$

where E_f is the elastic modulus of fiber; E_m is the elastic modulus of resin; ν_f is the Poisson's ratio of fiber; and ν_m is the Poisson's ratio of resin.

To calculate the transverse elastic modulus E_2 and in-plane shear modulus G_{12} , in this work the modified Tsai-Hahn model proposed by Huang [44] is used, as shown in Eqs. (7)–(11).

$$E_2 = \frac{E_f E_m [V_f + \eta_2 (1 - V_f)]}{E_m V_f + E_f \eta_2 (1 - V_f)} \quad (7)$$

$$\eta_2 = \frac{0.2}{1 - \nu_m} \left(1.1 - \sqrt{\frac{E_m}{E_f} + \frac{3.5 E_m}{E_f}} \right) (1 + 0.22 V_f) \quad (8)$$

$$G_{12} = \frac{G_f G_m [V_f + \eta_{12} (1 - V_f)]}{G_m V_f + G_f \eta_{12} (1 - V_f)} \quad (9)$$

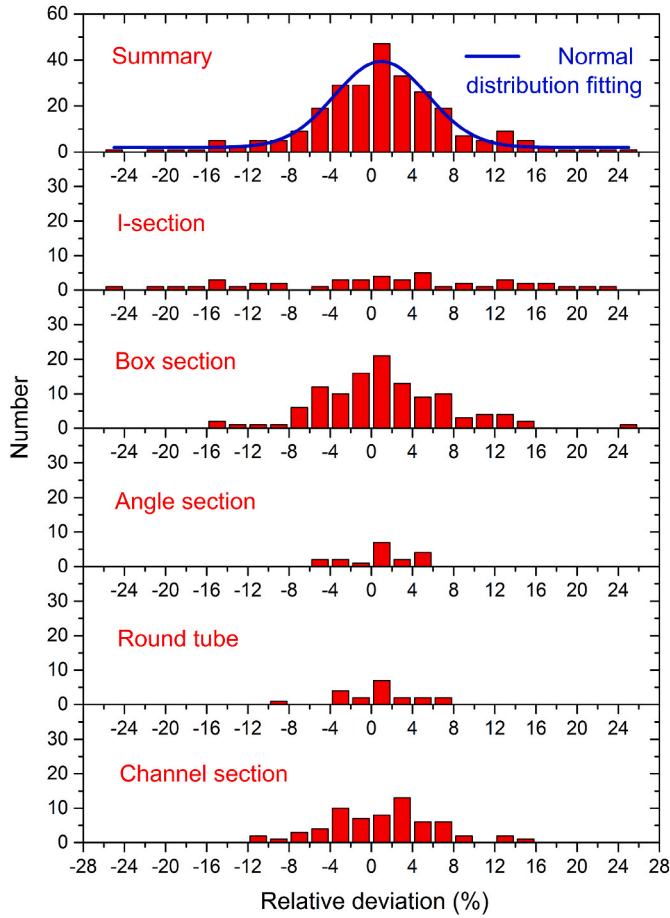


Fig. 7. Distributions of relative deviations.

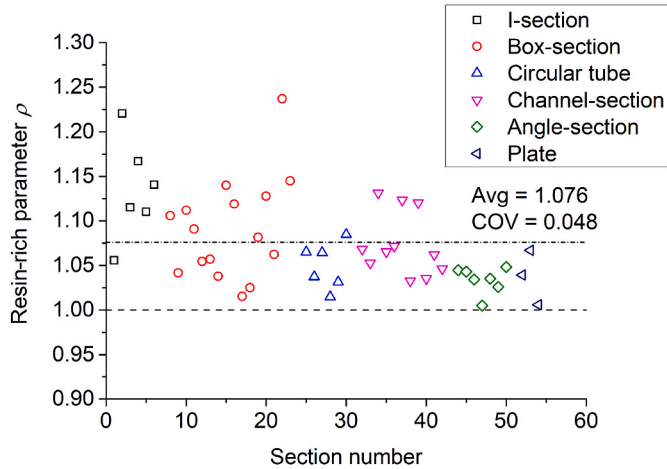


Fig. 8. Resin-rich parameters of tested sections.

$$\eta_{12} = 0.28 + \sqrt{\frac{E_m}{E_f}} \quad (10)$$

$$\nu_{21} = \nu_{12} \frac{E_2}{E_1} \quad (11)$$

where G_f is the shear modulus of fiber; G_m is the shear modulus of resin; η_{12} and η_{12} are the coefficients used for calculating E_2 and G_{12} , respectively; and ν_{21} is the minor Poisson's ratio.

In addition, to predict the longitudinal tensile strength F_L^t , Eq. (12) is

used [45].

$$F_L^t = X_f V_f + \frac{E_m}{E_f} X_f (1 - V_f) \quad (12)$$

where X_f is the tensile strength of fiber.

Prediction of longitudinal compressive strength F_L^c is based on the fiber buckling theory, and Eq. (13) is used [46].

$$F_L^c = \min \left(2V_f \sqrt{\frac{V_f E_m E_f}{3(1 - V_f)}}, \frac{G_f}{(1 - V_f)} \right) \quad (13)$$

Transverse tensile strength F_T^t can be predicted by Eq. (14) [46].

$$F_T^t = \frac{1 + V_f(1/\eta_y - 1)}{K_{my}} X_{mi} \quad (14)$$

where K_{my} is the stress concentration factor; η_y is the stress non-uniform coefficient; and X_{mi} is the smaller value of matrix tensile strength and interface strength.

There is still a lack of theoretical methods to predict the transverse compressive strength F_T^c . According to Shen et al. [47], F_T^c can be taken as 4 to 7 times of the transverse tensile strength F_T^t .

In-plane shear strength F_{LT} can be predicted by Eq. (15) [46].

$$F_{LT} = \frac{1 + V_f(1/\eta_s - 1)}{K_{ms}} S_{mi} \quad (15)$$

where K_{ms} is the stress concentration factor of shear stress; η_s is the stress non-uniform coefficient of shear stress; and S_{mi} is the smaller value of matrix shear strength and interface shear strength.

The above equations are used hereinafter to analyze the influence of NUFRD on the mechanical properties of GFRP sections.

4.3. Discount of mechanical property in resin-rich areas

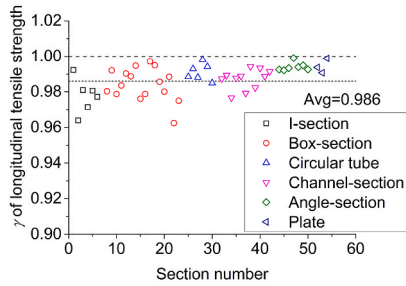
Based on the calculated resin-rich parameters and those prediction methods of mechanical properties, the material properties in resin-rich areas can be analyzed theoretically. In addition, the mechanical properties of the fiber and resins are provided by producer, as shown in Table 2.

Based on the test data, the mechanical properties corresponding to the maximum resin content and the average resin content of each group of data can be calculated. Then, the discount of mechanical properties in resin-rich areas can be obtained, which is described using the ratio of mechanical properties in resin-rich area to that of the whole section, defined as γ . The results of γ are shown in Fig. 9.

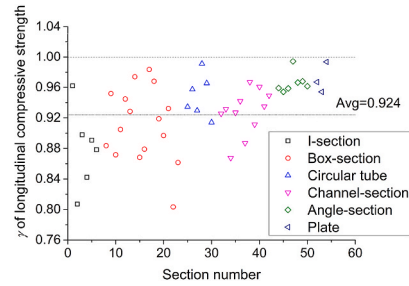
It shows that the most discounted property in resin-rich area is the longitudinal compressive strength. The minimum γ of longitudinal compressive strength is 0.807, and the average γ is 0.924. The discount of longitudinal tensile strength is smaller than that of longitudinal compressive strength, with average discount of 0.986. On the other hand, the resin-rich parts have negligible discounts in terms of the

Table 2
Mechanical properties of fiber and resin.

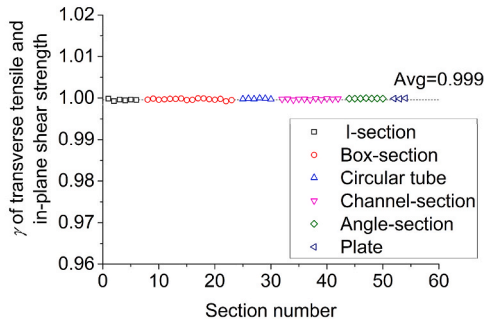
material	property	symbol	value
fiber	density/kg/m ³	ρ_f	2600
	Young's elastic modulus/GPa	E_f	81
	shear elastic modulus/GPa	G_f	33
	Poisson's ratio	ν_f	0.22
epoxy resin	density/kg/m ³	ρ_m	1300
	Young's elastic modulus/GPa	E_m	3.7
	shear elastic modulus/GPa	G_m	1.4
	Poisson's ratio	ν_m	0.35
vinyl ester resin	density/kg/m ³	ρ_m	940
	Young's elastic modulus/GPa	E_m	3.4
	shear elastic modulus/GPa	G_m	1.3
	Poisson's ratio	ν_m	0.35



(a) Discount of longitudinal tensile strength in resin-rich region



(b) Discount of longitudinal compressive strength in resin-rich region



(c) Discount of transverse tensile and in-plane shear strength in resin-rich area

Fig. 9. Discount of mechanical properties in resin-rich area.

transverse tensile and in-plane shear strength. It reflects that resin content has little relationship with transverse tensile and in-plane shear strength.

4.4. Modifications to mechanical center

The initial section eccentricity is known to be a common imperfection for structural elements, which shall be taken into consideration in the global buckling design of compressive members. For pultruded GFRP members, the section eccentricity has mainly resulted from two sources, including the initial deformation and non-uniform mechanical properties. The initial deformation can be measured directly, including the initial bending, initial twist, etc. These errors are strictly limited by design guides. For example, both Chinese standard GB/T 31539 and European standard EN 13706 specify the dimensional tolerances of pultruded GFRP profiles. In addition to initial deformation, the non-uniform mechanical properties can enlarge the section eccentricity, as shown in Fig. 10.

This section analyzes the influence of NUFRD on the section eccentricity. A second-order polynomial interpolation assumption was used to acquire the resin contents between the sampling points. Then, integration was used to calculate the eccentric distance. The local longitudinal elastic modulus $E_{x,y}$ was calculated based on the local resin content, according to Eq. (5). The location of mechanical central point (x_c, y_c) can be calculated via Eq. (16) and Eq. (17).

$$x_c = \frac{\int_A E_{x,y} x dA}{\int_A E_{x,y} dA} \quad (16)$$

$$y_c = \frac{\int_A E_{x,y} y dA}{\int_A E_{x,y} dA} \quad (17)$$

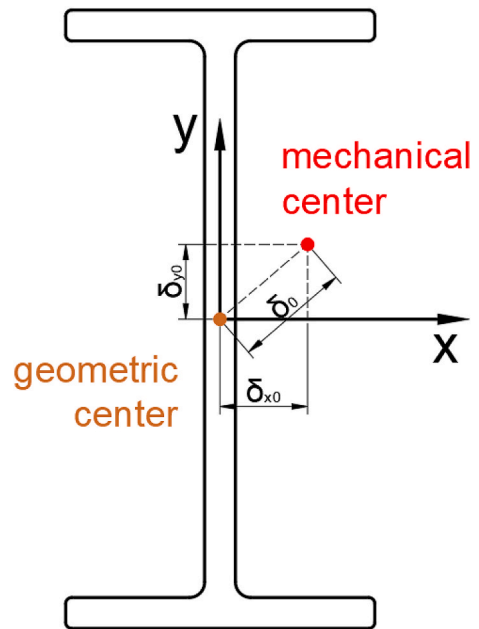


Fig. 10. Initial eccentric distance.

where A is the area of section; x and y are the coordinates of integration point.

Finally, the differences between the calculated central points and ideal central points are regarded as the eccentric distances $(\delta_{x0}, \delta_{y0})$ of the GFRP sections. In order to compare all the different GFRP sections,

the calculated results of eccentric distances are normalized against the radius of gyrations r_y and r_x , in which r_x and r_y are the radius gyrations about x-axis and y-axis, respectively. The calculated relative eccentric distances of tested sections are shown in Table 3. The number of tested GFRP plates is not statistically sufficient, and thus, the results of plates are not included. In Table 3, $|\delta_{x0}/r_y|$ and $|\delta_{y0}/r_x|$ are the average values about x-axis and y-axis, respectively. $\sqrt{(\delta_{x0}/r_y)^2 + (\delta_{y0}/r_x)^2}$ is the total value of relative eccentric distances.

As shown in Table 3, the relative eccentric distances are different for different sections. I-section profiles have the largest relative eccentric distances as compared to other sections. For I-sections, the radius of gyration about y-axis r_y is smaller than that about the x-axis r_x , which leads to the larger relative eccentric distance in x-direction. The angle-section profiles, channel-section profiles and circular tubes have smaller relative eccentric distances because of their less resin content non-uniformity.

5. Finite element modeling

Finite element modeling (FEM) was conducted to evaluate the influence of NUFRD on the structural behavior of pultruded GFRP profiles. In particular, axial compression members were modeled. The FE model was built via ABAQUS 6.14 [49]. In order to get a conservative result, for every section, tested member with largest resin content COVs is analyzed, including I-section $102 \times 51 \times 6.4$ mm, box-section $101.6 \times 101.6 \times 6.35$ mm, angle-section $75 \times 75 \times 10$ mm, circular tube 25×2.5 mm, and channel-section $139.7 \times 63.5 \times 6.35$ mm. The measured resin contents are specified in the model. For every section, models with three slenderness ratios (70, 100 and 130) are built. In order to define the coordinate-related material properties (including modulus and strength), field variables were used to consider the measured resin contents. In the material definition module, the pultruded GFRP was defined as a field variable depended orthotropic elastic material. The tabular data was specified to define the relationship between field variable and elastic modulus. Then, in the load module, the field variable was specified, which was the measured resin contents.

The I-section model is shown in Fig. 11 as an example. Shell element S4 with a size of 8 mm is used. The two end sections are pinned to reference points. The boundary conditions of two reference points are fixed and sliding, respectively. The displacement load was applied at the sliding reference point. The analysis was conducted via Riks step.

In addition, the material properties of fiber and resin are listed in Table 1. Then, the material properties of GFRP composites can be calculated by Eqs. (3)–(14). The relationship between resin content and modulus is also shown in Fig. 11. Then, in load module, the measured resin contents were input as field variable, as shown in Fig. 11. An assumption was made that the resin content variations of a section remained the same throughout the height of GFRP column.

In order to compare the results of models with different sections and lengths, normalized axial load-lateral displacement relationships are analyzed, as shown in Fig. 12. Normalized axial load is the ratio of axial load N to Euler critical load N_E , which shall be calculated by Eq. (18) [48,55]. Normalized lateral displacement is the ratio of lateral displacement x to section gyration radius r . Euler critical loads N_E are 22 kN, 10 kN, and 6 kN when the slenderness ratio λ is 70, 100 and 130,

Table 3 Average values (and COVs) of relative eccentric distances of different sections.

Section	$ \delta_{x0}/r_y $	$ \delta_{y0}/r_x $	$\sqrt{(\delta_{x0}/r_y)^2 + (\delta_{y0}/r_x)^2}$
I-section	0.020 (0.08)	0.004 (0.06)	0.021 (0.09)
box-section	0.011 (0.04)	0.010 (0.03)	0.012 (0.05)
angle-section	0.022 (0.02)	0.002 (0.01)	0.003 (0.02)
circular tube	0.001 (0.02)	0.004 (0.02)	0.004 (0.02)
channel-section	0.004 (0.01)	0.004 (0.02)	0.006 (0.02)

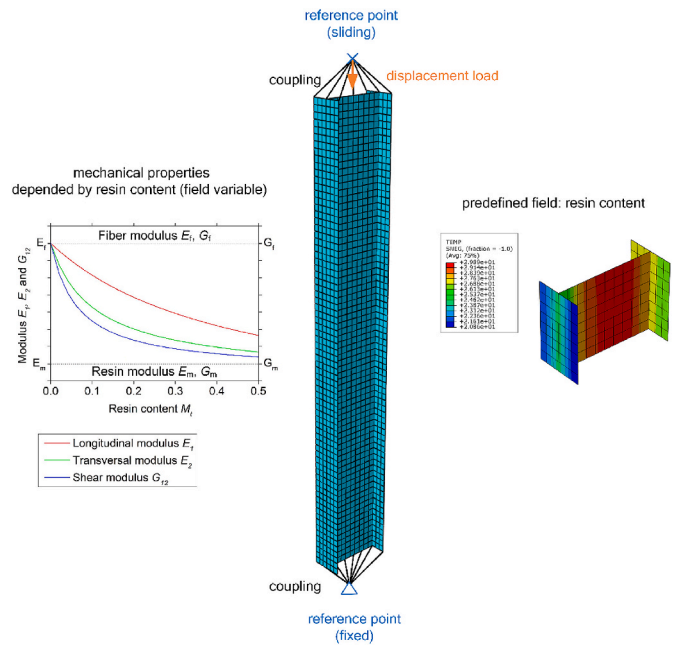


Fig. 11. Finite element modeling of pultruded GFRP I-section column with varying resin contents.

respectively. Same material properties are applied for different sections, so that different sections have the same Euler critical loads N_E .

$$N_E = \frac{\pi^2 E_L A}{\lambda^2} \tag{18}$$

where E_L is the longitudinal compressive elastic modulus; and λ is the slenderness ratio.

According to Fig. 12, the models with non-uniform material have higher lateral displacements for the same load. The members with a slenderness ratio of 70 have the lowest curves. Thus, it can be concluded that non-uniform material will decrease the compressive strength more obviously when compressive members have smaller slenderness ratio. As shown in section 4.4, the non-uniform material will add to the initial eccentric distance, so that the capacity of a compressive member is lower. I-section models with slenderness ratios λ of 70, 100 and 130 all have the significant decrease of axial loads. The influence on box-section model is more obvious when slenderness ratio is small. On the other hand, for angle-section, circular tube and channel-section, the differences between non-uniform material model and uniform material model are relatively smaller.

To analyze the influence of non-uniform material quantitatively, the moment where maximum compressive stress (usually located in mid-span section) reaches the material strength is captured, and the corresponding axial load is taken as the resistance of the column. Then, calculating the ratio of resistance of non-uniform material model to uniform material model, yields the resistance reduction factor. The results of resistance reduction factors are shown in Fig. 13.

As shown in Fig. 13, the resistance reduction factors of I-section are the lowest, followed by box-section. The reduction factors of angle-section, circular tube and channel-section are similar to each other and are all greater than 0.95. On the other hand, models with smaller λ values have lower reduction factors. The reduction factor of I-section with λ of 70 is the lowest, 0.88. Since only the GFRP sections with the largest COVs are analyzed by FEM, the obtained results are deemed conservative. This reduction factor can be directly adopted in the design of compressive members.

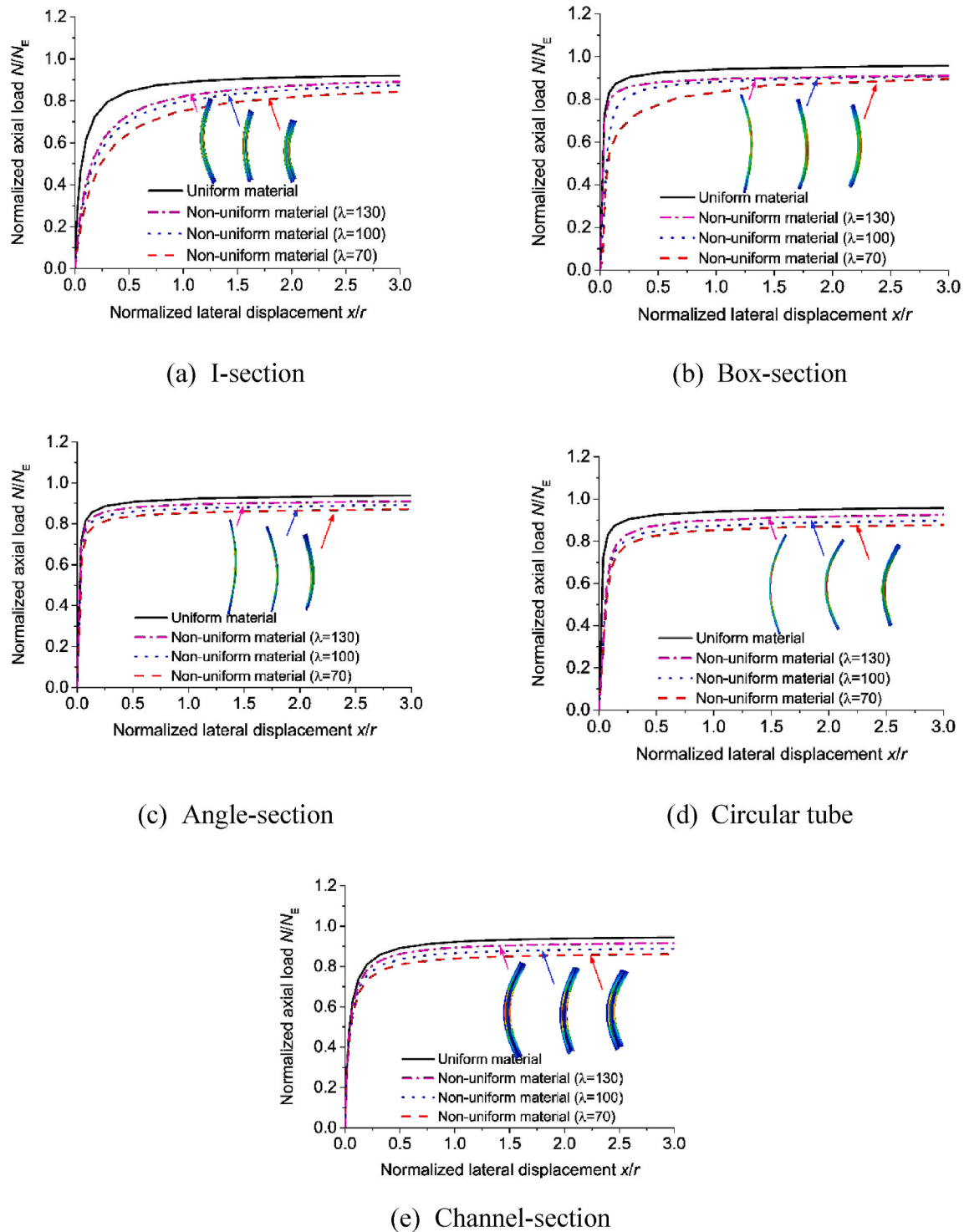


Fig. 12. Normalized axial load-lateral displacement relationships calculated by FEM.

6. Conclusions

The non-uniform resin contents of pultruded GFRP profiles were quantitatively identified and evaluated. The standard calcination method was used to measure the resin contents of 49 different sections provided by three manufacturers, including the I-sections, box-sections, angle-sections, circular tubes, channel-sections, and plates. The statistical analysis of the test results, the modified mechanical properties, and the resulting compressive behaviors of GFRP columns are addressed. Following conclusions can be drawn from this work:

- 1) The measured resin contents showed evident NUFRDs across each of the 49 pultruded GFRP sections. In particular, the resin contents of I-section profiles have the largest degree of non-uniformity, and the resin contents in the web are found to be larger than those in the flange. In addition, I- and box-section profiles have the largest COVs of the measured resin contents, by up to 0.16 and 0.12, respectively, whereas all the other sections, including the angle-sections, circular tubes and channel-sections, have COVs less than 0.10, showing a relatively good uniformity of fiber-resin distribution.

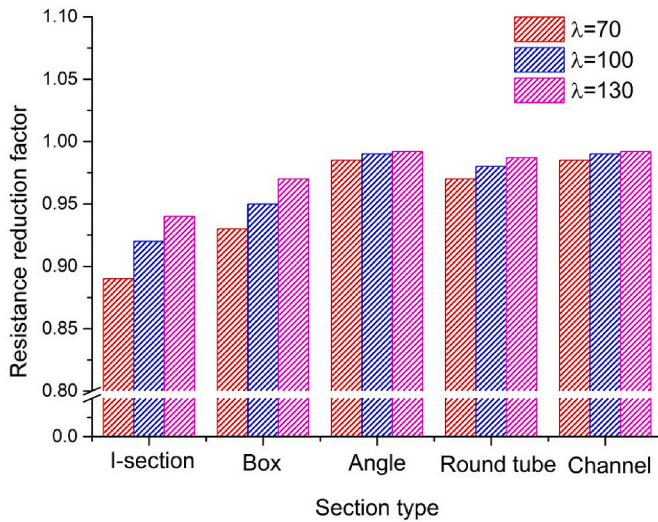


Fig. 13. Resistance reduction factors of compressive members calculated by FEM.

- 2) The statistical analysis of test results revealed that the accumulative distribution of relative deviations of resin contents are similar to the normal distribution. The adjusted R-square value of the normal distribution fitting is 0.94.
- 3) NUFRD is a type of inherent initial imperfection. It can lead to additional section eccentricity, by up to 0.021 for I-sections. This section eccentricity can further impact the compressive behavior of GFRP columns; that is, the critical buckling loads can be reduced.
- 4) FEM is built to analyze the influence of non-uniform material on compressive member. The resistance reduction of global buckling is

analyzed. The compressive member with a smaller slenderness ratio has lower resistance. The reduction factor of I-section with a slenderness ratio of 70 is the lowest, 0.88.

Data availability

All data, models, and code generated or used during the study appear in the submitted article.

Credit authorship contribution statement

Peng Feng: Conceptualization, Methodology, Supervision, Project administration, Funding acquisition, Writing - review editing. **Yuwei Wu:** Conceptualization, Methodology, Test, Investigation, Formal analysis, Visualization, Writing - original draft. **TianQiao Liu:** Methodology, Investigation, Visualization, Writing - original draft.

Declaration of competing interest

The authors declare that they have no known competing financial interests or personal relationships that could have appeared to influence the work reported in this paper.

Acknowledgements

This research was supported by the National Key R&D Program of China (2018YFB1501200), the National Natural Science Foundation of China (No. U2106219), and the grants from the Institute for Guo Qiang, Tsinghua University (2019GQG1004 and 2020GQC0004). The authors would like to acknowledge three manufacturers for material and test support, Nanjing Spare Composite Co., LTD, Nantong Composite Material Co., LTD, and Gold Bridge Composite (Beijing) Technology Co.,LTD.

Appendix A. Measured resin contents of pultruded GFRP sections

Table A.1

Resin contents of I-sections

No	Section size (h × b × t)/mm	Resin type	Manufacturer	Resin content/%									
				top flange			Web			bottom flange			average (COV)
				TF-1	TF-M	TF-2	W-1	W-2	W-3	BF-1	BF-M	BF-2	
1	100 × 70 × 6	epoxy	M 2	20.25	21.60	20.28	20.22	20.36	19.89	20.04	21.74	20.96	20.59 (0.03)
2	102 × 51 × 6.4	vinyl ester	M 1	23.96	28.80	23.23	32.42	33.74	33.43	22.15	27.65	23.39	27.64 (0.16)
3	120 × 70 × 8	epoxy	M 2	23.99	27.00	23.78	29.28	29.29	30.00	25.56	27.54	25.64	26.90 (0.08)
4	152 × 76 × 6.35	epoxy	M 1	25.66	27.75	21.55	33.70	33.99	31.90	28.68	30.05	28.82	29.12 (0.13)
5	152 × 80 × 10	epoxy	M 1	30.52	33.06	30.07	29.92	30.16	30.72	26.81	25.05	31.72	29.78 (0.08)
6	200 × 100 × 9.5	epoxy	M 1	26.07	27.44	27.77	30.28	30.16	29.75	20.76	24.72	21.93	26.54 (0.12)

Table A.2

Resin contents of box-sections

No	Section size (h × b × t)/mm	Resin type	Manufacturer	Resin content/%								
				Midpoint				Corner				average (COV)
				L-1	L-2	L-3	L-4	C-1	C-2	C-3	C-4	
1	25 × 25 × 3	epoxy	M 1	34.71	32.49	33.99	36.05	32.69	30.98	27.99	31.91	32.60 (0.07)
2	50 × 25 × 3	epoxy	M 1	32.71	-	32.32	-	34.00	34.47	32.22	32.83	33.09 (0.03)
3	75 × 35.5 × 6	epoxy	M 1	37.68	-	32.16	-	34.44	31.72	32.16	35.18	33.89 (0.06)
4	38 × 38 × 3.2	epoxy	M 1	30.69	33.87	31.28	30.95	32.34	29.74	30.31	29.24	31.05 (0.04)
5	38 × 38 × 5	epoxy	M 1	30.37	31.35	28.93	30.17	29.66	28.83	28.90	29.63	29.73 (0.03)
6	44 × 44 × 6	epoxy	M 1	37.58	37.75	35.14	34.57	36.92	35.49	33.71	34.57	35.72 (0.04)
7	50 × 50 × 4	epoxy	M 2	21.30	20.39	21.54	21.22	20.19	20.29	20.27	20.84	20.76 (0.02)
8	50.8 × 50.8 × 3.2	epoxy	M 1	32.69	28.41	27.09	26.93	31.96	29.32	26.65	26.30	28.67 (0.08)
9	50.8 × 50.8 × 6.35	epoxy	M 3	31.60	34.17	29.45	28.73	31.13	28.54	28.47	32.18	30.53 (0.06)

(continued on next page)

Table A.2 (continued)

No	Section size (h × b × t)/mm	Resin type	Manufacturer	Resin content/%								average (COV)
				Midpoint				Corner				
				L-1	L-2	L-3	L-4	C-1	C-2	C-3	C-4	
10	60 × 60 × 4.25	epoxy	M 1	30.15	31.15	31.26	30.93	31.29	29.94	30.64	31.16	30.82 (0.02)
11	68 × 95 × 6	epoxy	M 1	36.53	35.78	35.80	34.85	35.85	35.80	34.84	35.62	35.64 (0.01)
12	76.2 × 76.2 × 6.35	epoxy	M 1	28.51	31.97	30.94	31.31	27.29	27.20	29.53	29.74	29.56 (0.06)
13	76.2 × 76.2 × 6.35	vinyl ester	M 2	20.86	27.93	25.50	26.68	22.75	23.86	26.22	24.30	24.76 (0.09)
14	82 × 82 × 6.35	epoxy	M 1	33.67	31.72	32.55	32.67	30.95	30.78	29.60	31.61	30.74 (0.04)
15	101.6 × 101.6 × 6.35	vinyl ester	M 2	29.10	32.72	28.74	26.03	23.16	25.11	24.67	22.07	26.45 (0.12)
16	101.6 × 101.6 × 6.35	epoxy	M 1	31.00	26.50	26.54	30.35	27.88	29.31	28.29	33.39	29.16 (0.08)

Table A.3

Resin contents of angle-sections

No.	Section size (h × b × t)/mm	Resin type	Manufacturer	Resin content/%			average (COV)
				Corner	Midpoint		
				C	L-1	L-2	
1	50 × 50 × 3	epoxy	M 1	26.99	28.32	26.03	27.11 (0.03)
2	50.8 × 50.8 × 6.35	epoxy	M 2	32.38	31.07	29.69	31.05 (0.04)
3	55 × 55 × 4	epoxy	M 3	35.52	32.96	34.56	34.35 (0.03)
4	75 × 75 × 6	epoxy	M 1	33.03	32.65	32.91	32.86 (0.01)
5	75 × 75 × 10	epoxy	M 1	26.24	28.98	28.76	27.99 (0.04)
6	100 × 100 × 8	epoxy	M 1	35.70	34.87	33.82	34.80 (0.02)
7	101.6 × 101.6 × 6.35	vinyl ester	M 1	22.64	23.97	25.03	23.88 (0.04)

Table A.4

Resin contents of circular tubes

No.	Section size (D × t)/mm	Resin type	Manufacturer	Resin content/%								average (COV)
				C-1	C-2	C-3	C-4	C-5	C-6	C-7	C-8	
1	25 × 2.5	epoxy	M 1	26.98	–	29.77	–	30.45	–	31.64	–	29.71 (0.06)
2	30 × 2	epoxy	M 1	32.71	–	32.56	–	33.94	–	31.66	–	32.72 (0.02)
3	38 × 3	epoxy	M 1	31.83	–	34.00	–	30.46	–	31.50	–	31.95 (0.04)
4	40 × 4	epoxy	M 2	18.50	–	18.42	–	17.95	–	18.05	–	18.23 (0.01)
5	48.5 × 6.75	epoxy	M 1	30.69	–	30.56	–	32.51	–	32.58	–	31.59 (0.03)
6	82 × 3	epoxy	M 1	30.22	30.57	30.21	32.64	28.78	29.46	29.95	28.91	30.09 (0.04)

Table A.5

Resin contents of channel-sections

No.	Section size (h × b × t)/mm	Resin type	Manufacturer	Resin content/%							average (COV)
				top flange		Web			bottom flange		
				TF-C	TF-1	W-1	W-2	W-3	BF-C	BF-1	
1	35 × 23 × 4.5	epoxy	M 1	32.29	28.56	–	34.06	–	33.39	31.13	31.89 (0.06)
2	41.5 × 41.5 × 3.5	epoxy	M 1	37.56	35.38	–	35.41	–	38.55	36.19	36.62 (0.03)
3	76.2 × 25 × 6.35 × 6.35	vinyl ester	M 1	29.57	26.86	–	34.46	–	32.07	29.3	30.45 (0.09)
4	76.2 × 25 × 6.35	epoxy	M 1	33.14	34.63	–	33.09	–	30.76	30.91	32.51 (0.05)
5	88.9 × 38.1 × 4.76	vinyl ester	M 1	22.89	26.18	–	22.51	–	24.69	25.89	24.43 (0.06)
6	139.7 × 63.5 × 6.35	vinyl ester	M 1	26.80	31.25	–	26.51	–	26.15	28.36	27.81 (0.07)
7	150 × 50 × 6	epoxy	M 1	29.84	28.54	30.3	29.6	29.76	29.05	28.27	29.34 (0.02)
8	152.4 × 42.9 × 9.5 × 9.5	vinyl ester	M 1	20.61	21.84	25.36	24.44	23.26	20.84	22.09	22.63 (0.06)
9	200 × 60 × 8	epoxy	M 1	31.10	30.16	32.60	33.17	32.26	32.46	32.52	32.04 (0.03)
10	200 × 60 × 8	epoxy	M 1	32.04	26.96	32.55	30.9	30.7	30.81	30.56	30.65 (0.06)
11	280 × 70 × 12	epoxy	M 1	31.94	32.1	30.29	31.15	30.37	32.95	33.18	31.71 (0.02)

Table A.6
Resin contents of plates

No.	Section size (b × t)/mm	Resin type	Manufacturer	Resin content/%					
				L-1	L-2	L-3	L-4	L-5	average (COV)
1	40 × 5	epoxy	M 1	24.41	–	25.93	–	24.51	24.95 (0.03)
2	76.2 × 12.7	vinyl ester	M 1	20.48	–	22.15	–	19.65	20.76 (0.05)
3	136 × 6.35	epoxy	M 1	31.20	31.44	31.33	31.26	31.03	31.25 (0.01)

References

- Wang J, Feng P, Hao T, Yue Q. Axial compressive behavior of seawater coral aggregate concrete-filled FRP tubes. *Construct Build Mater* 2017;147:272–85.
- Feng P, Wang J, Wang Y, Loughery D, Niu D. Effects of corrosive environments on properties of pultruded GFRP plates. *Compos B Eng* 2014;67:427–33.
- Liu TQ, Liu X, Feng P. A comprehensive review on mechanical properties of pultruded FRP composites subjected to long-term environmental effects. *Compos B Eng* 2020;191:107958.
- Vedernikov A, Safonov A, Tucci F, Carlone P, Akhatov I. Pultruded materials and structures: a review. *J Compos Mater* 2020;0021998320922894.
- Starr TF, Ketel JAAP. *Composites and pultrusion. Pultrusion for engineers*. Cambridge: Woodhead Publishing Limited; 2000. p. 1–18.
- Gand AK, Chan TM, Mottram JT. Civil and structural engineering applications, recent trends, research and developments on pultruded fiber reinforced polymer closed sections: a review. *Front Struct Civ Eng* 2013;7(3):227–44.
- Jin F, Feng P, Ye L. Study on dynamic characteristics of light-weight FRP footbridge. In: *Advances in FRP composites in civil engineering*. Berlin, Heidelberg: Springer; 2011. p. 173–6.
- Zou X, Feng P, Wang J. Perforated FRP ribs for shear connecting of FRP-concrete hybrid beams/decks. *Compos Struct* 2016;152:267–76.
- Zou X, Feng P, Wang J, Wu Y, Feng Y. FRP stay-in-place form and shear key connection for FRP-concrete hybrid beams/decks. *Compos Struct* 2018;192:489–99.
- Zou X, Feng P, Bao Y, Wang J, Xin H. Experimental and analytical studies on shear behaviors of FRP-concrete composite sections. *Eng Struct* 2020;215:110649.
- Liu TQ, Feng P, Lu X, Yang JQ, Wu Y. Flexural behavior of a novel hybrid multicell GFRP-concrete beam. *Compos Struct* 2020;250:112606.
- Yang X, Bai Y, Ding F. Structural performance of a large-scale space frame assembled using pultruded GFRP composites. *Compos Struct* 2015;133:986–96.
- Xin H, Mosallam A, Liu Y, Xiao Y, He J, Wang C, et al. Experimental and numerical investigation on in-plane compression and shear performance of a pultruded GFRP composite bridge deck. *Compos Struct* 2017;180.
- Correia JR, Bai Y, Keller T. A review of the fire behaviour of pultruded GFRP structural profiles for civil engineering applications. *Compos Struct* 2015;127:267–87.
- Qiao P, Shan L. Explicit local buckling analysis and design of fiber-reinforced plastic composite structural shapes. *Compos Struct* 2005;70(4):468–83.
- Qiao P, Chen Q. Post-local-buckling of fiber-reinforced plastic composite structural shapes using discrete plate analysis. *Thin-Walled Struct* 2014;84:68–77.
- Mottram JT. Lateral-torsional buckling of thin-walled composite I-beams by the finite difference method. *Compos Eng* 1992;2(2):91–104.
- Fairuz AM, Sapuan SM, Zainudin ES, Jaafar CNA. Polymer composite manufacturing using a pultrusion process: a review. *Am J Appl Sci* 2014;11(10):1798.
- Minchenkov K, Vedernikov A, Safonov A, Akhatov I. Thermoplastic pultrusion: a review. *Polymers* 2021;13:180–2021.
- Korotkov R, Vedernikov A, Gusev S, Alajarmeh O, Akhatov I, Safonov A. Shape memory behavior of unidirectional pultruded laminate. *Compos Appl Sci Manuf* 2021;150:106609.
- Bai Y, Keller T. Shear failure of pultruded fiber-reinforced polymer composites under axial compression. *J Compos Construct* 2009;13(3):234–42.
- Yuksel O, Sandberg M, Hattel JH, Akkerman R, Baran I. Mesoscale process modeling of a thick pultruded composite with variability in fiber volume fraction. *Materials* 2021;14.
- Baran I, Cinar K, Ersoy N, Akkerman R, Hattel JH. A review on the mechanical modeling of composite manufacturing processes. *Arch Comput Methods Eng* 2017;24:365–95.
- Baran I, Tutum CC, Nielsen MW, Hattel JH. Process induced residual stresses and distortions in pultrusion. *Compos B Eng* 2013;51:148–61.
- Baran I, Akkerman R, Hattel JH. Modelling the pultrusion process of an industrial L-shaped composite profile. *Compos Struct* 2014;118:37–48.
- Koutsawa Y, Tiem S, Yu W, Frédrigo Addiego, Giunta G. A micromechanics approach for effective elastic properties of nano-composites with energetic surfaces/interfaces. *Compos Struct* 2016;159:278–87.
- Vedernikov A, Nasonov Y, Korotkov R, Gusev S, Akhatov I, Safonov A. Effects of additives on the cure kinetics of vinyl ester pultrusion resins. *J Compos Mater* 2021;00219983211001528.
- Vedernikov A, Safonov A, Tucci F, Carlone P, Akhatov I. Modeling spring-in of Lshaped structural profiles pultruded at different pulling speeds. *Polymers* 2021;13(16):2748.
- Safonov A, Gusev M, Saratov A, Konstantinov A, Sergeichev I, Konev S, et al. Modeling of cracking during pultrusion of large-size profiles. *Compos Struct* 2020;235:111801.
- Baran I, Straumit I, Shishkina O, Lomov SV. X-ray computed tomography characterization of manufacturing induced defects in a glass/polyester pultruded profile. *Compos Struct* 2018;195(JUL):74–82.
- Nguyen TT, Chan TM, Mottram JT. Influence of boundary conditions and geometric imperfections on lateral-torsional buckling resistance of a pultruded FRP I-beam by FEA. *Compos Struct* 2013;100:233–42.
- Antin KN, Laukkanen A, Andersson T, Smyl D, Vilaça P. A multiscale modelling approach for estimating the effect of defects in unidirectional carbon fiber reinforced polymer composites. *Materials* 2019;12(12):1885.
- Ascione F. Influence of initial geometric imperfections in the lateral buckling problem of thin walled pultruded GFRP I-profiles. *Compos Struct* 2014;112:85–99.
- Poulton M, Sebastian W. Taxonomy of fibre mat misalignments in pultruded GFRP bridge decks. *Compos Appl Sci Manuf* 2020:106239.
- Bank LC, Yin J. Failure of web-flange junction in postbuckled pultruded I-beams. *J Compos Construct* 1999;3(4):177–84.
- Liu TQ, Harries KA. Flange local buckling of pultruded GFRP box beams. *Compos Struct* 2018;189:463–72.
- Liu TQ, Yang JQ, Feng P, Harries KA. Determining rotational stiffness of flange-web junction of pultruded GFRP I-sections. *Compos Struct* 2020;236:111843.
- Turvey GJ, Zhang Y. Characterisation of the rotational stiffness and strength of web-flange junctions of pultruded GRP WF-sections via web bending tests. *Compos Appl Sci Manuf* 2006;37(2):152–64.
- Ascione L, Berardi VP, Giordano A, Spadea S. Pre-buckling imperfection sensitivity of pultruded FRP profiles. *Compos B Eng* 2015;72:206–12.
- Hsiao KT, Gangireddy S. Investigation on the spring-in phenomenon of carbon nanofiber-glass fiber/polyester composites manufactured with vacuum assisted resin transfer molding. *Compos Appl Sci Manuf* 2008;39(5):834–42.
- Exner W, Hein R, Mahrholz T, Wierach P, Monner HP, Sinapius M. Impact of nanoparticles on the process-induced distortions of carbon fiber reinforced plastics: an experimental and simulative approach. *J Appl Polym Sci* 2019;136(5):47031.
- Vedernikov A, Tucci F, Carlone P, Gusev S, Konev S, Firsov D, et al. Effects of pulling speed on structural performance of L-shaped pultruded profiles. *Compos Struct* 2021;255:112967.
- Boukhili R, Boukehili H, Daly HB, Gasmi A. Physical and mechanical properties of pultruded composites containing fillers and low profile additives. *Polym Compos* 2006;27(1):71–81.
- Huang ZM. Micromechanical strength formulae of unidirectional composites. *Mater Lett* 1999;40(4):164–9.
- Rosen BW. Tensile failure of fibrous composites. *AIAA J* 1964;2(11):1985–91.
- Tsai SW, Hahn HT. *Introduction to composite materials*. Routledge; 2018.
- Shen GL, Hu G, Liu B. *Mechanics of composite materials*. second ed. Beijing, China: Science and Technology; 2013.
- Asce. *Pre-standard for load and resistance factor design of pultruded fiber reinforced polymer structures*. 2010.
- Abaqus 6.14. ABAQUS documentation. Providence, RI, USA: Dassault Systèmes; 2014.
- Astm D6641/D6641M-09. Standard test method for compressive properties of polymer matrix composite materials using a combined loading compression. West Conshohocken, PA: CLC Test Fixture; 2009.
- GB/T 1448. Fiber-reinforced plastics composites-Determination of compressive properties. Standardization Administration of China; 2005 [in Chinese].
- GB/T 2577. Test method for resin content of glass fiber reinforced plastics. Standardization Administration of China; 2005 [in Chinese].
- GB/T 31539. Pultruded fiber reinforced polymer composites structural profiles. Standardization Administration of China; 2015 [in Chinese].
- ISO 1172. Textile-glass-reinforced plastics — prepreps, moulding compounds and laminates — determination of the textile-glass and mineral-filler content — calcination methods. 1996.
- CECS 692 T/. Technical specification for structure of pultruded fiber reinforced polymer composites. 2020 [in Chinese].